Bioluminescent Nanoluciferase–Furimamide Complex: A Theoretical Study on Different Protonation States

Mehdi Sahihi, Juan Sanz Garcia, Isabelle Navizet

Bioluminescent Nanoluciferase-Furimamide Complex: A Theoretical Study on Different Protonation States

Mehdi Sahihi, Juan Sanz García and Isabelle Navizet**

MSME, Univ Gustave Eiffel, UPEC, CNRS, F-77454, Marne-la-Vallée, France

***Corresponding authors:**

Mehdi Sahihi and Isabelle Navizet

MSME, Univ Gustave Eiffel, UPEC, CNRS, F-77454, Marne-la-Vallée, France

Tel: +33 (0) 1 60 95 72 42

Fax: +33 (0) 1 60 95 77 99

E-mail: mehdi.sahihi@u-pem.fr and isabelle.navizet@u-pem.fr

Abstract

Luminescence of furimamide is 150 times brighter than oxidized luciferins in firefly and renilla luciferase. However, we do not have a clear understanding of the structure, function and dynamic behavior of the nanoluciferase-furimamide complex. Here, for the first time, the absorption and emission proprieties of eight different possible light emitter forms of furimamide were investigated using the TD-DFT method in the gas phase and aqueous solution. The emission oscillator strengths in the gas phase showed that emission transition may be forbidden for some forms, and fluorescence would not occur. Besides, the charge transfer (CT) as well as the orbitals involved in the transitions were analyzed. Furthermore, molecular docking results showed that furimamide is situated inside the central cavity (β-barrel) of nanoluciferase. Analysis of the trajectory of molecular dynamics (MD) simulations suggested a less compact structure of protein in the presence of furimamide in comparison to its apo form. The QM/MM spectroscopic proprieties of one form in the binding site of nanoluciferase were investigated. The evolution of the ESs of furimamide in the binding pocket of the protein confirmed that after photoexcitation and during the relaxation of the system, a crossing point between the first two singlet ESs exists. Thus, the initially populated S2 (a $\pi \rightarrow \pi^*$ transition) becomes the first singlet excited state.

1. Introduction

Bioluminescence process is catalyzed by luciferase protein and converts the chemical energy into the visible light. This natural phenomenon could be seen in a wide variety of organisms from bacteria to jellyfish[1,2]. The potential biomedical applications of this phenomenon such as the study of protein-protein interactions[3], the investigation of genetic regulation and cell signaling[4], BRET-based biosensors and molecular imaging[5] have attracted considerable interest among scientists. In this regard, investigating the bioluminescence mechanism and spectroscopic properties of the light emitter species are very interesting[6-9]. Recently, a new bioluminescence system including a small luciferase, nanoluciferase (NLuc), with molecular weight of 19.1 kDa and a highly specific synthetic substrate, furimazine, has become commercially available[10]. Luminescence of the oxidized form of furimazine, furimamide (Fur), is 150 times brighter than the one observed from the oxidized luciferins in firefly and renilla luciferase (FLuc and RLuc, respectively), and is adenosine triphosphate (ATP)-independent[10]. Nowadays, NLuc-furimazine complex is widely used to investigate protein–protein and ligand–protein interactions[11], regulation of gene expression and intracellular cascades[12], molecular imaging[13] and photodynamic therapy[14,15]. In most of the bioluminescence mechanisms, luciferase binds a substrate and the emitter is generated in the first singlet ES by decomposition of a cyclic peroxide and release of CO_2 (Scheme 1)[16-23]. Finally, emitter decays to the GS by emitting light in the visible range of wavelength.

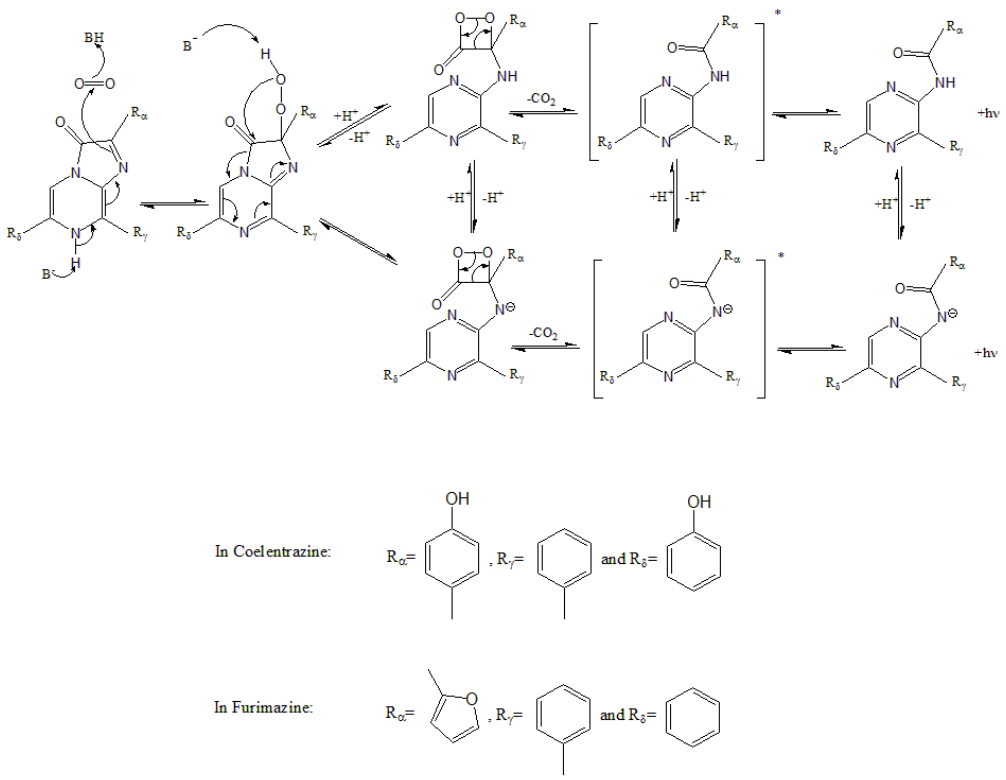

Scheme 1. General bioluminescence mechanism in coelenterazine-like systems. B^- and BH could be either OH^- and H_2O (or deprotonated and protonated form of a residue in protein binding site), respectively. Previous calculation on Cypridina bioluminescence suggests that dioxetanone decomposition is likely from the neutral form[21]. There is no information about furimazine.

It is notable that the emission color can differ from blue to red depending on various factors such as nature of the light emitter[24], pH[25], presence of bivalent metal ions[26], temperature[27], and luciferase mutations[28]. In contrast to the large amount of experimental and theoretical data available on the FLuc structure and function[29,30], we do not have a clear understanding of the structure, function and dynamic behavior of the NLuc-Fur complex. To our knowledge, there is no comprehensive study on the fluorescence and bioluminescence of furimazine. Here, we have

studied the absorption and fluorescence of eight protonated and deprotonated forms of Fur, *i.e.* three neutral forms, the amide anion, three pyrazine cations and the pyrazine dication (Figure 1). In order to do so, density functional theory (DFT) and its time-dependent (TD-DFT) version have been used. The investigations have been done in the gas phase and aqueous solution. Furthermore, we have clarified the interaction of furimazine with NLuc and the stability of Fur-NLuc complex using molecular docking and MD simulation methods, respectively. The spectroscopic properties of the form A of Fur in the binding site of NLuc were investigated using QM/MM calculations.

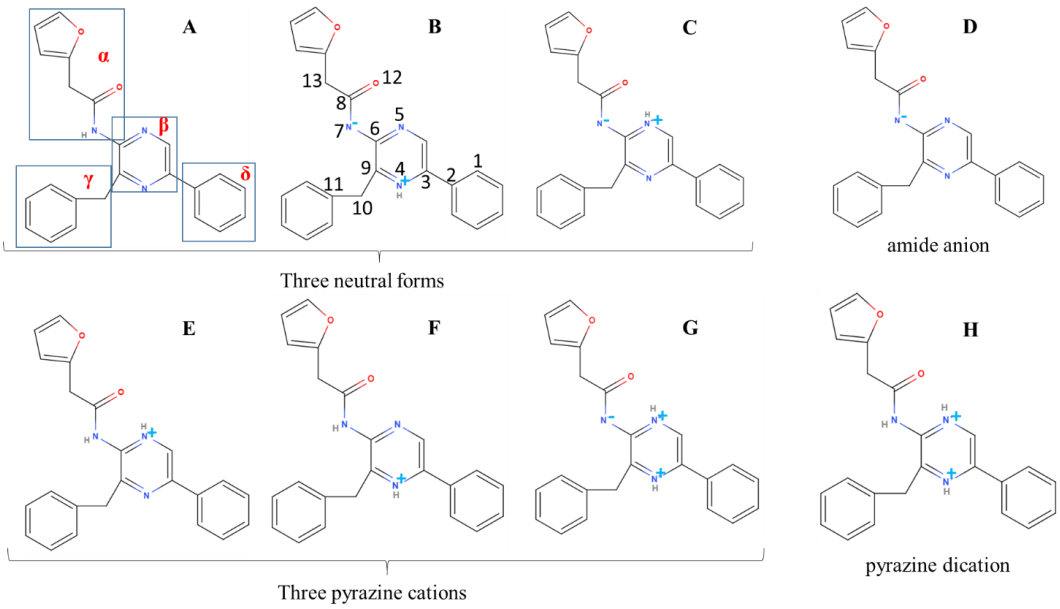

Figure 1. Different forms of Fur according to the protonation states of nitrogen atoms. A, B and C are neutral; B and C are zwitterions; D is an anion; E, F, G and H are cations; E and F are charged +1e and G shows two +1e charges and one -1e and H is a dication.

2. Theoretical Method

2.1. QM calculations

All quantum mechanical (QM) calculations were performed with Gaussian 09 package[31] using DFT and TD-DFT for the GS and ESs, respectively. The long-range corrected CAM-B3LYP[32] functional which is commonly used to describe charge transfer (CT) excitations was used together with the Pople's polarization valence-triple-ζ 6-311G(2d,p)[33-35] basis set in order to optimize ground and ES geometries as well as to determine the absorption and fluorescence spectra. Previous studies on similar systems have shown that CAM-B3LYP method can reproduce the emission and absorption maxima in reasonable agreement with the experimental results[24, 36, 37]. In all TD-DFT calculations, the first five singlet ESs were considered to study the absorption. The brightest ES was selected and further optimized. The TD-DFT vertical transition was calculated and reported as emission. Calculations on the systems in water were done with implicit solvation using the polarizable continuum model (PCM)[38]. It has been shown that the PCM model is not ideal to simulate the effect of the water solvent on the spectra[39], but it is a cheap model and usually used for taking into account the water surrounding for a low computational cost. Also, Natural Bond Orbital (NBO)[40] analysis was performed to study the emitter electronic structures in water phase.

2.2. Molecular Docking

Docking study was carried out to indicate the NLuc binding site for furimazine. The crystal structure of NLuc (PDB ID: 5IBO) was taken from the Brookhaven Protein Data Bank (http://www.rcsb.org/pdb). The resolution and R-value of this structure are 1.95 Å and 0.250, respectively. Before using the coordinates of the crystallographic structure for docking procedure, the missing side chains and protonation state of the histidine residues were determined using

WHATIF web interface[41]. The obtained structure from the output of WHATIF server was subjected to 50 ns of MD simulation (See section 2.3 for details of MD) and its final structure was selected as input file for molecular docking procedure using AutoDock 4.2.6 software. The ligand used (furimazine in its neutral form seen in scheme 1) was firstly optimized at the CAM-B3LYP/6-311G(2d,p) level of theory. Flexible ligand docking was carried out using Gasteiger charges and the implemented empirical free energy function and the Lamarckian Genetic Algorithm[42]. AutoGrid was used to calculate the grids and a blind docking with 126 lattice points along X, Y, and Z axes was performed to find the binding site of furimazine on NLuc. Grid point spacing was set to 0.375 Å. This setting allows the ligand to be able to rotate freely. In the next step, the center of the grid box was located at the center of binding site and a second docking was performed using a cubic box with 60 lattice points. 250 docking runs with 25,000,000 energy evaluations for all runs were performed.

2.3. MD simulation

The NLuc-furimazine complex with the best scoring function corresponding to the negative free binding energy (from molecular docking calculations) was selected and furimazine was replaced by the optimized structure of Fur (A form). The prepared structure of NLuc-Fur complex was considered as the initial conformation for the MD simulation study. GROMACS 2018 package[43] and GROMOS 53a6 force field[44] were used to carry out all MD studies. Moreover, the force field parameters for Fur were taken from prodrg web server[45] and the atomic partial charges were corrected based on the Lemkul's method[46]. In parallel, a system of NLuc without ligand was also prepared. Apo NLuc and NLuc-Fur complex were located in a cubic box with periodic boundary

conditions in the three directions. The protein was placed in the center of the box and the minimum distance between solute surface and the box was set to 1.0 nm. The box was filled with SPC water molecules[47], and the solvated systems were neutralized by adding appropriate amounts of sodium ions (Na^+). The systems were energy minimized using the steepest descent method and were equilibrated for 1 ns in NVT followed by 1 ns in NPT ensembles. Finally, a 50 ns MD simulation was carried out at 1 bar and 300 K. Berendsen thermostat[48], Parrinello-Rahman barostate[49, 50], 1 nm cut-off for van der Walls (vdW) and Coulomb interactions were applied. Also, the particle mesh Ewald (PME) method[51, 52] was used for long range electrostatics. The leap-frog algorithm with a time step of 2 fs was used to integrate the equations of motion. Finally, the atomic coordinates were recorded to the trajectory file every 0.5 ps for later analysis.

2.4. QM/MM calculations

The clustering analysis of the 50 ns MD trajectory was performed using GMX Cluster module of GROMACS and the best structure of the most populated cluster was selected for hybrid QM and molecular mechanical (MM) (QM/MM method) optimization followed by a TD-DFT/MM calculation considering the first five ESs (absorption study). Subsequently, an optimization of the brightest state afforded the minimum geometries of the ES was used for the emission study. All these calculations were performed using the hybrid Own N-layered Integrated Molecular Orbital and molecular Mechanics (ONIOM) method[53] as implemented in the Gaussian 09 quantum chemistry package[31, 54] (please see figure S1 for details of ONIOM calculations). The MM was described using the AMBER force field while QM method ((TD) CAM-B3LYP/6-311G(2d,p)) was chosen for the emitter. All residues, ions and the water molecules farther than 5 Å of the

emitter were frozen during the QM/MM calculations. The QM/MM calculations were performed with mechanical embedding. Electrostatic embedding gives similar results (see Table S3). Mechanical embedding was chosen in order to investigate the crossing intersection between the ESs during the relaxation of the brightest ES. Use of AMBER force field for the description of MM interactions instead of GROMOS force field as in the MD simulation was motivated by the easy availability of this former in Gaussian 09 software. On the other hand, 50 ns MD simulations of NLuc were done with AMBER and GROMOS force fields. Comparison of the obtained trajectories showed that these two force fields give similar global trajectories for NLuc. (see Figure S2).

3. Results and Discussion

3.1. Gas-phase model

Optimized geometries of the eight emitter forms (see forms in Figure 1) in gas phase at their GSs, predicted by CAM-B3LYP/6-311G(2d,p) method are shown in Figure S3.

The structural characteristics of optimized ground states (GSopts) and optimized excited states (ESopts) are reported in the Supporting Information (Tables S1 and S2, respectively). The atom numbering is presented in Figure 1. In all structures, the amide dihedral angles (O12-C8-N7-C13) are almost the same in GSopts and ESopts and differ less than 5.4° from a planar conformation of the carbonyl group. In all structures, except B and C, the C8-O12 bond distance for the ESopts is less than 1.23 Å, which corresponds to a CO double bond character. The highest occupied molecular orbital (HOMO) and the lowest unoccupied molecular orbital (LUMO) of all emitters are shown in Figure 2. The electronic density of the HOMO is located on the pyrazine and phenyl

groups (β and δ parts in Figure 1) of neutral and anionic structures while in the case of the cationic forms, the electronic density is located on the furamide group (α part in Figure 1). However, the electron density of the LUMO is mainly located on the phenyl and/or the pyrazine moieties for all the structures. The electronic transitions for the first five ESs were predicted at the TD CAM-B3LYP/6-311G(2d,p) level of theory using the GSopts geometries (Table 1). The wavelengths corresponding to the electronic transitions with oscillator strengths values (*f*) are hereafter designated as calculated absorption maxima wavelengths. For each emitter, optimization of the brightest ES was performed to obtain ESopt structures. Subsequently, a TD-DFT calculation was performed in order to determine the emission wavelength. The emission oscillator strength (*f*) values of the structures decrease as D>C> E>A>F>B>G. The *f* value corresponding to the emission of B form is very small and for G is zero. Hence, the emission transition in the gas phase may be forbidden for B and G forms and fluorescence may not occur. It should be mentioned that the analysis of the oscillator strength is not the only factor determining the emission probability but gives an information on the radiation probability. Emission quantum yield should be determined by taking into account the radiation probability and all the possible relaxation channels. Hence, if all the non-radiative pathways are non-accessible emission, a transition will still be possible even with low oscillator strength. An exploration of the fluorescence of Fur in the aqueous phase and in the presence of protein is essential.

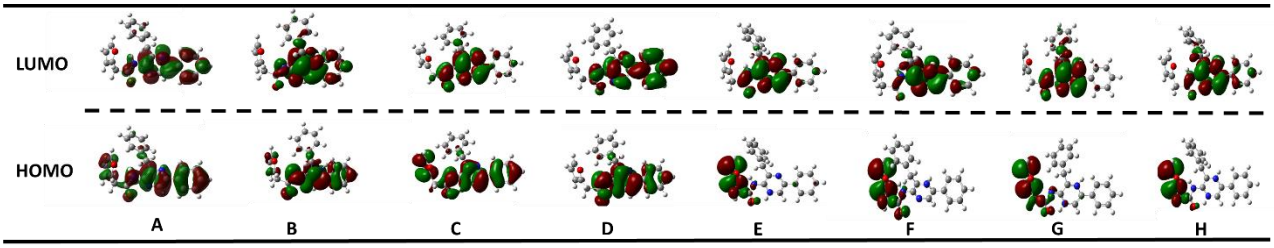

Figure 2. Calculated frontier MOs of structures A to H at the GS optimized geometry in gas phase, using CAM-B3LYP/6-311G(2d,p) method.

Table 1. Vertical excitation wavelengths at the GSopt geometries (absorption, λ_{abs} in nm) of the first five singlet ESs, emission (λ_{em} in nm) of the optimized ES at the ESopt geometries (emission) (and λ_{em} in nm) and corresponding oscillator strengths (*f*) in gas phase.

Structure	GSopt		ESopt		Structure	GSopt		ESopt	
	λ_{abs}	*f*	λ_{em}	*f*		λ_{abs}	*f*	λ_{em}	*f*
A/S1	290.21	0.0951	383.32	0.1199	**E/S1**	340.06	0.2903	409.26	0.1961
S2	272.05	0.4748			**S2**	313.36	0.0012		
S3	256.21	0.0620			**S3**	298.75	0.0134		
S4	244.88	0.1758			**S4**	291.91	0.0100		
S5	237.21	0.0089			**S5**	288.12	0.0109		
B/S1	420.63	0.1841			**F/S1**	365.85	0.0149		
S2	356.41	0.0024	623.33	0.0002	**S2**	346.06	0.3157	724.38	0.0011
S3	298.71	0.6233			**S3**	308.31	0.1305		
S4	296.06	0.0074			**S4**	283.69	0.0205		
S5	279.91	0.0294			**S5**	280.82	0.0119		
C/S1	321.46	0.3309	388.82	0.2833	**G/S1**	472.00	0.0437	1161.58	0.0000
S2	315.44	0.0367			**S2**	400.54	0.1661		
S3	273.48	0.2420			**S3**	365.02	0.0172		
S4	271.33	0.2792			**S4**	343.59	0.0121		
S5	252.41	0.0012			**S5**	335.83	0.0055		
D/S1	332.05	0.5501	385.05	0.3538	**H/S1**	642.03	0.0084	*a*	*a*
S2	307.17	0.2641			**S2**	501.73	0.0764		
S3	301.71	0.0583			**S3**	474.39	0.0158		
S4	276.87	0.0074			**S4**	446.84	0.2362		
S5	266.30	0.0327			**S5**	404.77	0.0047		

[a]*Calculation not converged.*

3.2. Water-phase PCM model

The predicted absorption (and emission) wavelengths of the emitters at the optimized ground (and excited) state geometries in water (PCM) are summarized in Table 2. For most of the emitters, the S1←S0 transition, which corresponds mainly to an excitation from the HOMO to the LUMO is the brightest transition with a large *f* value. Moreover, the results show that all the structures, except H form, are fluorescent in aqueous medium. The emission oscillator strength (*f*) values of the structures decrease from D to H as D>A>F>B>E>C>G>H. As in the gas phase, structure D (anionic form) has the maximum *f* value. However, the *f* values of the structures are higher than the corresponding values in gas phase.

Natural bond orbital (NBO) atomic charges analysis in water phase (PCM model) are reported in Table 3. NBO ground and ESs charges were calculated for the different moieties of the molecules. For neutral forms (structures A and B), anionic form (structure D) and dicationic form (structure H), negative charge is transferred from the acetamide part to the pyrazine (α to β moiety) upon electronic excitation. Moreover, for cationic emitters, negative charge is transferred from benzyl to pyrazine (δ to β moiety). Also, for zwitterionic structure C, CT direction is from acetamide and benzyl parts to pyrazine (α and δ to β moiety).

Table 2. Vertical excitation wavelengths at the GSopt geometries (absorption, λ_{abs} in nm) of the first five singlet ESs, emission (λ_{em} in nm) of the optimized ES at the ESopt geometries (emission) (and λ_{em} in nm) and corresponding oscillator strengths (*f)* in water phase (PCM model).

Structure	GSopt		ESopt		Structure	GSopt		ESopt	
	λ_{abs}	*f*	λ_{em}	*f*		λ_{abs}	*f*	λ_{em}	*f*
A/S1	293.16	0.4343	357.72	0.8303	**E/S1**	326.01	0.6519	388.15	0.6189
S2	277.99	0.4613			**S2**	293.13	0.0010		
S3	254.51	0.1670			**S3**	278.27	0.0210		
S4	244.75	0.1560			**S4**	265.75	0.2092		
S5	237.80	0.0268			**S5**	264.62	0.4030		
B/S1	400.33	0.4525			**F/S1**	337.50	0.6875	420.39	0.7744
S2	328.33	0.0073	366.88	0.7286	**S2**	308.55	0.0622		
S3	299.16	0.8833			**S3**	278.99	0.0406		
S4	278.75	0.0145			**S4**	266.65	0.0906		
S5	269.42	0.0258			**S5**	265.35	0.0091		
C/S1	336.62	0.6802	402.53	0.5914	**G/S1**	398.34	0.4730	515.56	0.4700
S2	311.33	0.0024			**S2**	369.38	0.0054		
S3	278.37	0.6739			**S3**	320.30	0.0329		
S4	268.56	0.0151			**S4**	302.57	0.0345		
S5	246.34	0.0012			**S5**	290.12	0.0203		
D/S1	328.99	0.6962	400.30	0.9035	**H/S1**	406.10	0.5389	706.21	0.0020
S2	292.28	0.2640			**S2**	390.31	0.0675		
S3	288.19	0.3134			**S3**	361.00	0.0283		
S4	260.71	0.0247			**S4**	339.44	0.0028		
S5	245.61	0.0163			**S5**	330.16	0.0078		

The reactions extracted from the Born–Haber thermodynamic cycle method (Scheme 2) were used to estimate the equilibrium constants of protonation and deprotonation during the transformation from one form to the other (Scheme 3). The p*K* and pK^* values (for the GS and ES, respectively) were calculated in water using equations 1-4[55, 56] and are collected in Table 4. These values are used to determine the relative stability of different forms of Fur.

Table 3. Natural bond orbital (NBO) atomic charges analysis in water phase (PCM model) at the CAM-B3LYP/6-311G(2d,p) and TD CAM-B3LYP/6-311G(2d,p) levels of theory. α, β, γ and δ are the moieties represented in Figure 1. The NBO were calculated for GS in the GSOpts and for ES in the ESopts.

Structure		**α**	**β**	**γ**	**δ**	**Structure**		**α**	**β**	**γ**	**δ**
A	GS	-0.161	0.133	0.012	0.016	**E**	GS	0.005	0.825	0.070	0.100
	ES	-0.080	0.009	0.030	0.041		ES	0.017	0.552	0.048	0.383
	Δ(ES-GS)	**0.081**	**-0.124**	**0.018**	**0.025**		**Δ(ES-GS)**	**0.012**	**-0.273**	**-0.022**	**0.283**
B	GS	-0.671	0.623	0.047	0.001	**F**	GS	-0.060	0.865	0.087	0.108
	ES	-0.548	0.541	0.040	-0.033		ES	0.031	0.573	0.081	0.315
	Δ(ES-GS)	**0.123**	**-0.082**	**-0.007**	**-0.034**		**Δ(ES-GS)**	**0.091**	**-0.292**	**-0.006**	**0.207**
C	GS	-0.693	0.641	0.033	0.019	**G**	GS	-0.514	1.298	0.128	0.088
	ES	-0.606	0.471	0.019	0.116		ES	-0.427	1.111	0.080	0.236
	Δ(ES-GS)	**0.087**	**-0.170**	**-0.014**	**0.097**		**Δ(ES-GS)**	**0.087**	**-0.187**	**-0.048**	**0.148**
D	GS	-0.884	-0.018	-0.024	-0.074	**H**	GS	0.118	1.516	0.157	0.209
	ES	-0.690	-0.187	-0.015	-0.108		ES	0.799	0.989	0.162	0.050
	Δ(ES-GS)	**0.194**	**-0.169**	**0.009**	**-0.034**		**Δ(ES-GS)**	**0.681**	**-0.527**	**0.005**	**-0.159**

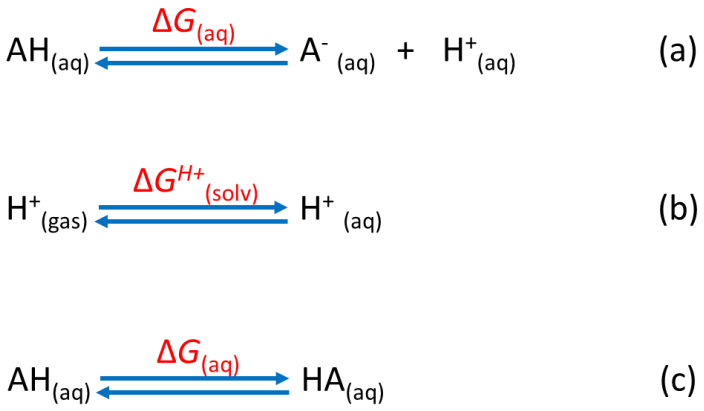

Scheme 2. Equations used for the calculations of the thermodynamic constants for reactions depicted in Scheme 3. Scheme 2a describes the deprotonation of couples AH/A^- that corresponds to couples: A/D, B/D, C/D, E/A, E/B, E/C, F/A, F/B, F/C, G/A, G/B, G/C, H/E, H/F, H/G. Scheme 2b describes the part of the Born-Haber thermodynamic cycle corresponding to the solvation of proton used to take the experimental values. Scheme 2c describes a proton transfer form one part to another part of the molecule.

$$\Delta G_{(aq)} = G^{H^+}_{(aq)} + G^{A^-}_{(aq)} - G^{AH}_{(aq)} \quad (1)$$

or

$$\Delta G_{(aq)} = G^{HA}_{(aq)} - G^{AH}_{(aq)} \quad (2)$$

$$G^{H^+}_{(aq)} = \Delta G^{H^+}_{(solv)} + G^{H^+}_{(gas)} \quad (3)$$

$$pK = \Delta G_{(aq)}/2.303RT \quad (4)$$

The Gibbs free energies were calculated by numerical vibrational frequency analysis of GSopts and ESopts at the CAM-B3LYP/6-311G(2d,p) level of theory using Gaussian 16 package[57]. The

free energy of the H^+ in the gas phase, $G^{H+}_{(gas)}$ and its solvation-free energy, $\Delta G^{H+}_{(solv)}$ were inferred from experiments and were taken to be -6.28 kcal.mol^{-1} and -263.98 kcal.mol^{-1}, respectively[58, 59]. A -RT Ln(24.46) should be included to account for the transfer of a solute molecule from a 1 atm gas phase into a 1 M solvent standard state[60].

Table 4. Computed GS and ES transformation (or dissociation) constants (pK and pK^*, respectively) of transformations represented in scheme 3 between different forms of Fur in water.

K_i	reaction	pK	pK^*
1	H = F	-15.98	-1.95
2	H = E	-21.02	-4.44
3	H = G	-9.20	-6.94
4	F = E	-5.04	-2.49
5	E = G	11.82	-2.50
6	F = A	-6.34	1.47
7	G = C	-8.79	0.93
8	F = B	12.31	17.40
9	E = A	-1.30	3.96
10	E = C	3.03	-1.57
11	G = B	5.53	22.39
12	A = B	18.66	15.93
13	B = C	-14.32	-21.47
14	A = D	19.28	11.33
15	B = D	0.62	-4.60
16	C = D	14.94	16.87

The results show a very complex equilibrium between the different forms in water. The deprotonation constants of pyrazine cations to neutral forms (pK_6-pK_{11}) show that, in the GS, the

reaction are in favor of populating neutral forms A and C (specially form A) and depopulating B form and protonated forms. Furthermore, strong negative values of pK_1-pK_3 and negative values of pK^*_1-pK^*_3 show that the deprotonated dicationic form H is negligible in all pH and in both electronic states. Overall, forms A and C of Fur appear to be dominant in all pH range in aqueous solution in GS and ES, respectively.

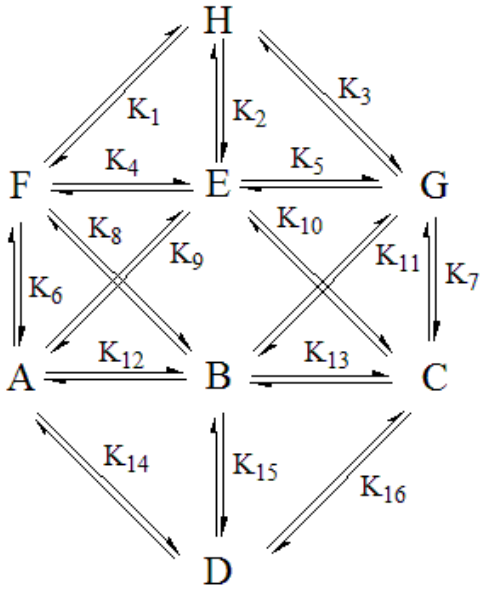

Scheme 3. Different forms of Fur and their respective transformation and dissociation equilibrium constants. The reaction' schemes have been simplified. Reactions transforming a compound in one line to the form of the line below, correspond to a deprotonation, i.e. F = A + H^+. Reactions transforming compound to a compound in the same line correspond to a proton transfer from one part to another part of the molecule and the two forms have same charge: H is double protonated, F, E and G are cations of charge +1, A, B and C are neutral and D is anionic.

3.3. *NLuc-ligand model*

Molecular docking is a powerful method to predict and obtain primarily insight about the stable structure of receptor-ligand complex. Due to the lack of crystal structure of NLuc-furimazin complex, molecular docking study was carried out to find out the preferred location and conformation of furimazine on NLuc. The docking poses and their related binding energies of first 5 complexes with the most negative free binding energy from the molecular docking calculations have been presented in figure S4. The results indicate that furimazine is situated inside the central cavity (β-barrel) of NLuc. Figure 3 represents the binding pose of furimazine inside the protein and the amino acid residues which surround it in the binding site. The standard binding free energy ($\Delta G°$) of this interaction is about -9.82 kcal·mol^{-1}. The molecular complex system shows a H-bond (with Arg162 residue) and hydrophobic interactions between furimazine and NLuc. These interactions may have key roles in the stability of the system. Furthermore, the binding pose for anionic form of furimazine was compared to its neutral form. Figure S5 shows that the two forms (neutral and anionic) are docked in the same cavity and differ only from the dihedral angle of the connection of R_α cycle. In the pose of the neutral form an H-bond with the Arg162 is observed and the protonated (neutral) form has more negative value for binding energy (-9.82 and -9.75 kcal.mol^{-1} for neutral and anionic forms, respectively).

The molecular structure of furimazine in the binding site was modified to A form of Fur and a 50 ns MD simulation was carried out on the NLuc-Fur complex. In parallel, a 50 ns MD simulation of apo-NLuc structure was also performed. The stability of the system was examined by means of RMS deviations (RMSD), RMS fluctuations (RMSF), solvent accessible surface area (SASA) of biomacromolecule and radius of gyration (R_g) for NLuc and NLuc-Fur systems (Figure S6).

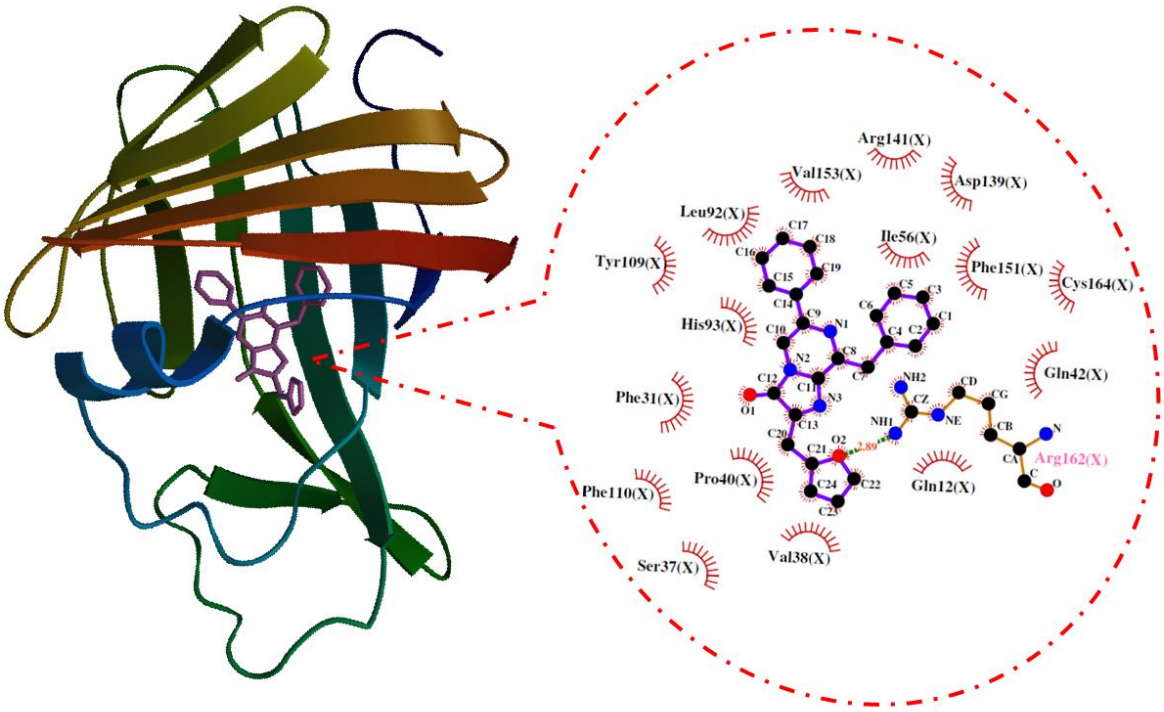

Figure 3. Docking pose of NLuc-furimazine complex. H-bond and hydrophobic interactions are represented as green dashed lines and red arcs, respectively.

Analysis of the trajectories shows that both systems are stable and their RMSD reach equilibrium and fluctuate around its mean value after about 35 ns of simulation time. It can be clearly seen that the R_g and SASA increase upon binding of Fur suggesting a less compact structure of NLuc in comparison to its apo form. Moreover, local protein mobility and its conformational adjustments were analyzed by calculating the time averaged RMSF values of apo-NLuc and NLuc-Fur complex and were plotted against residue numbers based on the last 15 ns of the trajectories. The RMSF values of the residues that are in contact with Fur are lower than in the simulation of apo-NLuc. This confirms the structural rigidity of the binding site during the simulation time.

Also, time dependence of the distance between O atom in furamide ring (α part in Figure 1) of Fur and H atom of NH_2 group in Arg 162 was investigated during last 15 ns of the trajectory (Figure S7). The results show that the average value for the selected atoms is about 3.45 Å and Arg 162 is susceptible to participate in an H-bond that stabilizes the compound. Furthermore, during the dynamics there are some possibilities of H-bond between N7-H of Fur and O atom of Tyr 109 (see figure S7). Tyr 109 could be H-Shuttle or H-donor/acceptor in the proton transfer mechanism.

The clustering analysis of the 50 ns MD trajectory (for NLuc-Fur complex) was performed using GMX Cluster module of GROMACS and the best structure of the most populated cluster was selected as the starting geometry for QM/MM calculations (Figure S1). The prepared NLuc-Fur structure was optimized both in GS and for the brightest ES at QM/MM level and electronic transitions were calculated.

Figure S8 shows the geometrical changes of Fur during the QM/MM optimization procedure of its GS. Table 5 represents the predicted absorption and emission wavelengths of Fur at GSopt and ESopt geometries in the presence of NLuc. Furthermore, we observed a blue shift of the absorption maximum wavelength of Fur in the protein cavity in comparison to the ones computed in water and gas phases. Further calculations using the electronic embedding model within the ONIOM framework have been performed in order to analyze the possible changes on the absorption/emission spectra. The results from these calculations show that there are no significant changes in the spectra after full optimization of the GS and ES using the electronic embedding model, see Table S3 for further information.

Natural transition orbitals (NTOs)[62] was used for further investigations and characterization of the transitions. In NTO representation, each particular transition is characterized by a single pair of hole-particle orbitals.

Table 5. Vertical excitation wavelengths at the GSopt geometry (absorption, λ_{abs} in nm) of the first five singlet ESs, emission (λ_{em} in nm) of the optimized ES at the ESopt geometry (emission) (and λ_{em} in nm) and corresponding oscillator strengths (*f)* of the Fur molecule in the presence of NLuc (QM/MM calculations).

Structure	GSopt		ESopt	
	λ_{abs}	*f*	λ_{em}	*f*
A/S1	279.97	0.0280	348.79	0.1316
S2	265.00	0.4541		
S3	242.05	0.0296		
S4	235.43	0.0429		
S5	232.23	0.0263		

After photoexcitation, the system relaxes throughout the potential energy surface (PES) of the initially populated π→π* state (the brightest state and corresponding to the second singlet at the Franck-Condon (FC) geometry). During the relaxation of the system, a crossing point between the first two singlet ESs is found not far from the FC geometry (see Figure 4). The NTOs computed at the FC geometry (see Table 6) show that the electronic nature of the first singlet ES, S1, corresponds to an n→π* state while the initially populated ES, S2, is a π→π* state. The NTOs computed right after the crossing point show that S1 has become the π→π* transition and S2 has become the n→π* transition as expected. Assuming that the system pursues the relaxation following the 'steepest descent', the macromolecular complex reaches a minimum at the S1 PES. Then, the system relaxes to the ground state by fluorescence, emitting photons with energy of about 3.5 eV. It is worth noticing that also in the gas phase and in water (PCM) a crossing point

between states S1 and S2 is found near the Franck-Condon geometry using three different methods: i) the standard optimization algorithm used by Gaussian[63], ii) a steepest descent optimization as implemented in Gaussian and iii) a steepest descent minimization using NTOs (SDNTO)[64, 65] (Figures S9 and S10). Moreover, we find here the results that are consisted with the Kasha's rule which states that the photon emission (fluorescence or phosphorescence) occurs in appreciable yield only from the lowest excited state of a given multiplicity[66] (the first singlet excited state in Figure 4). However, this rule could be overcome as we can see in the case of compounds F and B in gas phase and compound B in water (see tables 1 and 2).

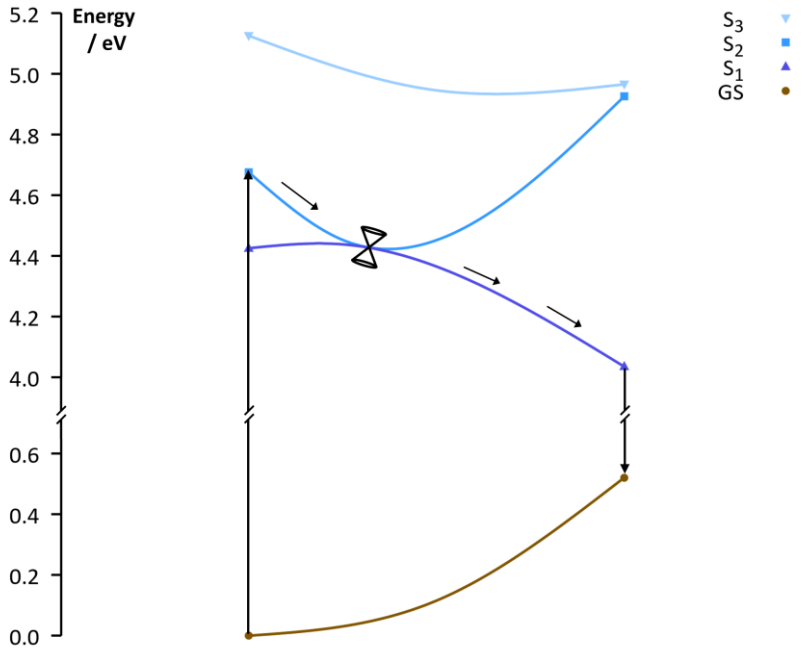

Figure 4. Evolution of the relative energies for the GS and ESs of form A of Fur (black arrows represent the systems pathway during the fluorescence process, and the double-cone pictogram represents the S1/S2 crossing point).

Table 6. The NTOs computed at the FC geometry and after the crossing point for three first singlet ESs of Fur.

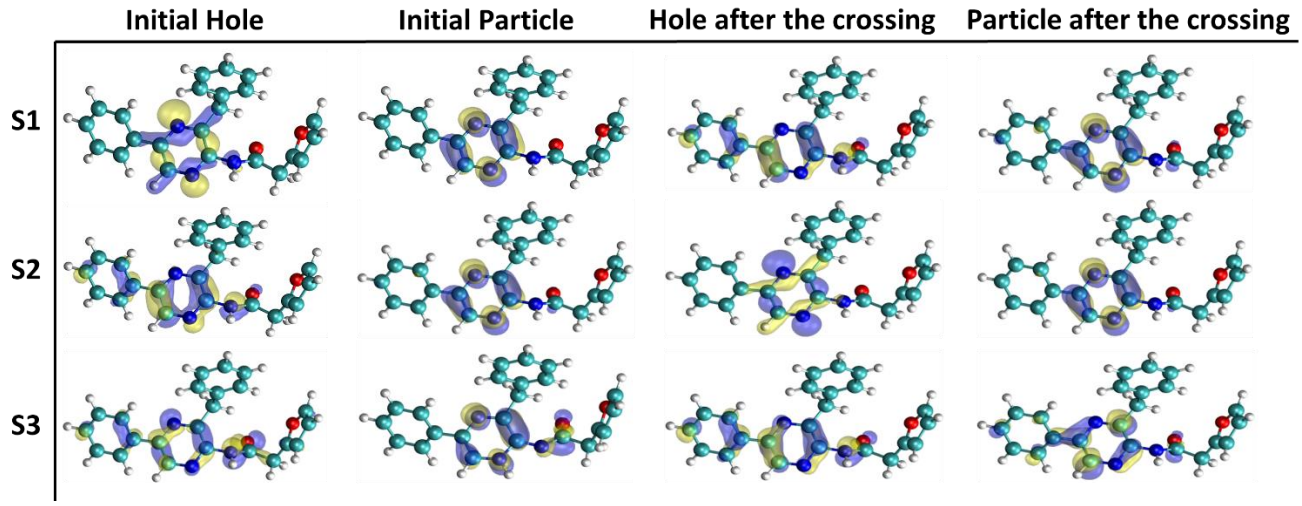

4. Conclusions

In the present study, the absorption and emission spectra of eight different possible light emitters of Fur: three neutral forms, one amide anion, three pyrazine cations and one pyrazine dication were investigated using TD-DFT calculations in the gas phase and aqueous solution. Likewise, two-layer ONIOM calculations were employed to perform QM/MM studies to investigate the absorption and emission spectra of a neutral form of Fur in the binding site of NLuc.

The emission oscillator strength (*f*) values showed that the emission transition in the gas phase is forbidden for some forms of Fur. Also, the *f* values of the structures in gas phase are generally lower than the corresponding values in water. The charge distributions for the ground and ESs of all the emitters were predicted in the water phase and the calculated charges showed that for A, B, D and H forms negative charge is transferred from the acetamide to the pyrazine moiety upon electronic excitation. However, for structures E, F and G, negative charge is transferred from benzyl to pyrazine moiety. Analysis of equilibrium constant (from equations extracted from Born-Haber cycle) showed that neutral form of furimamide appears to be dominant in all pH range in aqueous solution in both ground and ES. Furthermore, molecular docking results showed that furimazine is situated inside the central cavity (β-barrel) of NLuc with the standard binding free energy of about −9.82 kcal·mol^{-1}. The molecular docking also showed that H-bond and hydrophobic interactions stabilize the complex of NLuc-furimazine. Besides, the MD simulation results verified the structural rigidity of the binding site and decreasing the compactness of NLuc due to the binding of Fur. Finally, the full analysis of the ONIOM calculations on the form A in NLuc, the evolution of the ESs and the NTOs of furimamide in the binding pocket of the protein showed that during the photoexcitation-emission process, the first two singlet ESs cross each other. These results helps to better understand the photo activity of the NLuc-furimamide system and will be used to further investigation on the bioluminescence of furimazine-NLuc system, notably by investigate the conformation resulting from the bioluminescent reaction that can be different from the one resulting from photoexcitation.

Supporting Information

Figures for details of QM/MM calculations, analysis of MD simulation trajectories, optimized structures of the different protonated forms of Fur in their GS in gas phase, different poses obtained using molecular docking calculations, geometrical changes of Fur due to their binding to NLuc using ONIOM calculations and evolution of the relative energies for the GS and ESs of form A of Fur in gas and water phases. Tables for structural characteristics of optimized ground states (GSopts), optimized excited states (ESopts) and QM/MM electronic embedding model.

Acknowledgment

MS and IN are grateful to the French Agence Nationale de la Recherche (Grant: ANR-BIOLUM ANR-16-CE29-0013)

References

[1] Shimomura, O. *Bioluminescence: Chemical Principles and Methods;* World Scientific: Singapore, 2012.

[2] Herring, P. J. *Bioluminescence in Action;* Academic Press: London New York, 1978.

[3] Song, G.; Wu, Q. P.; Xu, T.; Liu, Y. L.; Xu, Z. G.; Zhang, S. F.; Guo, Z. Y. Quick preparation of nanoluciferase-based tracers for novel bioluminescent receptor-binding assays of protein hormones: Using erythropoietin as a model. *J. Photochem. Photobiol. B* **2015**, *153*, 311–316.

[4] Yasuzaki, Y.; Yamada, Y.; Ishikawa, T.; Harashima. H. Validation of Mitochondrial Gene Delivery in Liver and Skeletal Muscle via Hydrodynamic Injection Using an Artificial Mitochondrial Reporter DNA Vector. *Mol. Pharm.* **2015**, *12*, 4311– 4320.

[5] Stacer, A. C.; Nyati, S.; Moudgil, P.; Iyengar, R.; Luker, K. E.; Rehemtulla, A.; Luker, G. D. NanoLuc Reporter for Dual Luciferase Imaging in Living Animals. *Mol. Imaging* **2013**, *12*, 1–13.

[6] Zimmer, M. Green Fluorescent Protein (GFP): Applications, Structure, and Related Photophysical Behavior. *Chem. Rev.* **2002**, *102*, 759–782.

[7] Baubet, V.; Le Mouellic, H.; Campbell, A. K.; Lucas-Meunier, E.; Fossier, P.; Brúlet, P. Chimeric green fluorescent protein-aequorin as bioluminescent Ca^{2+} reporters at the single-cell level. *Proc. Natl. Acad. Sci. U. S. A.* **2000**, *97*, 7260–7265.

[8] Fraga, H. Firefly luminescence: A historical perspective and recent developments. *Photochem. Photobiol. Sci.* **2008**, *7*, 146-158.

[9] Kaskova, Z. M.; Tsarkova, A. S.; Yampolsky, I. V. 1001 lights: luciferins, luciferases, their mechanisms of action and applications in chemical analysis, biology and medicine. *Chem. Soc. Rev.* **2016**, *45*, 6048–6077.

[10] Hall, M. P.; Unch, J.; Binkowski, B. F.; Valley, M. P.; Butler, B. L.; Wood, M. G.; Otto, P.; Zimmerman, K.; Vidugiris, G.; Machleidt, T.; et al. Engineered Luciferase Reporter from a Deep Sea Shrimp Utilizing a Novel Imidazopyrazinone Substrate. *ACS Chem. Biol.* **2012**, *7*, 1848–1857.

[11] Verhoef, L. G.; Mattioli, M.; Ricci, F.; Li, Y. C.; Wade, M. Multiplex detection of protein–protein interactions using a next generation luciferase reporter. *Biochim. Biophys. Acta* **2016**, *1863*, 284–292.

[12] Lackner, D. H.; Carre, A.; Guzzardo, P. M.; Banning, C.; Mangena, R.; Henley, T.; Oberndorfer, S.; Gapp, B. V.; Nijman, S. M.; Brummelkamp, T. R.; et al. A generic strategy for CRISPR-Cas9-mediated gene tagging. *Nat. Commun.* **2015**, *6*, 10237-10243.

[13] Germain-Genevois, C.; Garandeau, O.; Couillaud, F. Detection of Brain Tumors and Systemic Metastases Using NanoLuc and Fluc for Dual Reporter Imaging. *Mol. Imaging Biol.* **2016**, *18*, 62– 69.

[14] Shramova, E. I.; Proshkina, G. M.; Chumakov, S. P.; Khodarovich, Y. M.; Deyev, S. M. Flavoprotein miniSOG Cytotoxisity Can Be Induced By Bioluminescence Resonance Energy Transfer. *Acta Naturae* **2016**, *8*, 118–123.

[15] Shramova, E. I.; Proshkina, G. M.; Deyev, S. M.; Petrov, R. V. Flavoprotein miniSOG BRET-induced cytotoxicity depends on its intracellular localization. *Dokl. Biochem. Biophys.* **2017**, *474*, 228–230.

[16] White, E. H.; Rapaport, E.; Seliger, H. H.; Hopkins, T. A. The Chemi- and Bioluminescence of Firefly Luciferin: An Efficient Chemical Production of Electronically Excited States. *Bioorg. Chem.* **1971**, *1*, 92−122.

[17] Deluca, M.; McElroy, W. D. Kinetics of the firefly luciferase catalyzed reactions. *Biochemistry* **1974**, *13*, 921-925.

[18] Navizet, I.; Liu, Y. J.; Ferre, N.; Roca-Sanjua, N. D.; Lindh, R. The Chemistry of Bioluminescence: An Analysis of Chemical Functionalities. *Chem. Phys. Chem.* **2011**, *12*, 3064−3076.

[19] García-Iriepa, C.; Gosset, P.; Berraud-Pache, R.; Zemmouche, M.; Taupier, G.; Dodzi-Dorkenoo, K.; Didier, P.; Léonard, J.; Ferré, N.; Navizet, I. Simulation and analysis of the spectroscopic properties of oxyluciferin and its analogues in water. *J. Chem. Theo. Comput.* **2018**, *14*, 2117-2126.

[20] Min, C. G.; Ferreira, P. J. O.; Pinto da Silva, L. Theoretically obtained insight into the mechanism and dioxetanone species responsible for the singlet chemiexcitation of Coelenterazine. *J. Photochem. Photobiol. B: Biol.* **2017**, *174*, 18-26.

[21] Pinto da Silva, L.; Pereira, R. F. J.; Magalhães, C. M.; Esteves da Silva, J. C. G. Mechanistic Insight into *Cypridina* Bioluminescence with a Combined Experimental and Theoretical Chemiluminescent Approach. *J. Phys. Chem. B* **2017**, *121*, 7862-7871.

[22] Magalhães, C. M.; Esteves da Silva, J. C. G.; Pinto da Silva, L. Study of coelenterazine luminescence: Electrostatic interactions as the controlling factor for efficient chemiexcitation. *J. Lumin.* **2018,** *199*, 339-347.

[23] Magalhães, C. M.; Esteves da Silva, J. C. G.; Pinto da Silva, L. Comparative study of the chemiluminescence of coelenterazine, coelenterazine-e and *Cypridina* luciferin with an experimental and theoretical approach. *J. Photochem. Photobiol. B: Biol.* **2019**, *190*, 21-31.

[24] Min, C. G.; Li, Z. S.; Rena, A. M.; Zoua, L. Y.; Guoc, J. F.; Goddard, J. D. The fluorescent properties of coelenteramide, a substrate of aequorin and obelin. *J. Photochem. Photobiol. A: Chem.* **2013**, *251*, 182-188.

[25] Ando, Y.; Niwa, K.; Yamada, N.; Enomoto, T.; Irie, T.; Kubota, H.; Ohmiya, Y.; Akiyama, H. Firefly Bioluminescence Quantum Yield and Colour Change by pH-Sensitive Green Emission. *Nat. Nat. Photonics* **2008**, *2*, 44−47.

[26] Wang, Y.; Kubota, H.; Yamada, N.; Irie, T.; Akiyama, H. Quantum Yields and Quantitative Spectra of Firefly Bioluminescence with Various Bivalent Metal Ions. *Photochem. Photobiol.* **2011**, *87*, 846−852

[27] Mochizuki, T.; Wang, Y.; Hiyama, M.; Akiyama, H. Robust Red Emission Spectra and Yields in Firefly Bioluminescence against Temperature Changes. *Appl. Phys. Lett.* **2014**, *104*, 213704.

[28] Wang, Y.; Akiyama, H.; Terakado, K.; Nakatsu, T. Impact of Site-Directed Mutant Luciferase on Quantitative Green and Orange/ red Emission Intensities in Firefly Bioluminescence. *Sci. Rep.* **2013**, *3*, 2490.

[29] Navizet, I.; Liu, Y. J.; Ferré, N.; Xiao, H. Y.; Fang, W. H.; Lindh, R. Color-Tuning Mechanism of Firefly Investigated by Multi-Configurational Perturbation Method. *J. Am. Chem. Soc.* **2010**, *132*, 706–712.

[30] Navizet, I.; Roca-Sanjuán, D.; Yue, L.; Liu, Y. J.; Ferré, N.; Lindh, R. Are the Bio- and Chemiluminescence States of the Firefly Oxyluciferin the Same as the Fluorescence State? *Photochem. Photobiol.* **2013**, *89*, 319–325.

[31] Frisch, M. J.; Trucks, G. W.; Schlegel, H. B.; Scuseria, G. E.; Robb, M. A.; Cheeseman, J. R.; Scalmani, G.; Barone, V.; Mennucci, B.; Petersson, G. A.; et al. GAUSSIAN 09, Revision D. 01, Gaussian, Inc., Wallingford, CT, 2013.

[32] Yanai, T.; Tew, D. P.; Handy, N. C. A new hybrid exchange-correlation functional using the Coulomb-attenuating method (CAM-B3LYP). *Chem. Phys. Lett.* **2004**, *393*, 51–57.

[33] Hehre, W.J.; Ditchfield, R.; Pople, J. A. Self-Consistent Molecular Orbital Methods. XII. Further Extensions of Gaussian-Type Basis Sets for Use in Molecular Orbital Studies of Organic Molecules. *J. Chem. Phys.* **1972**, *56*, 2257-2261.

[34] Hariharan, P. C.; Pople, J. A. The influence of polarization functions on molecular orbital hydrogenation energies. *Theo. Chim. Acta* **1973**, *28*, 213-222.

[35] Francl, M. M.; Pietro, W. J.; Hehre, W. J. Self-consistent molecular orbital methods. XXIII. A polarization-type basis set for second-row elements. *J. Chem. Phys.* **1982**, *77*, 3654-3665.

[36] Chen, S. F.; Ferré, N.; Liu, Y. J. QM/MM Study on the Light Emitters of Aequorin Chemiluminescence, Bioluminescence, and Fluorescence: A General Understanding of the Bioluminescence of Several Marine Organisms. *Chem. Eur. J.* **2013**, *19*, 8466-8472.

[37] Berraud-Pache, R.; Navizet, I. QM/MM calculations on a newly synthesised oxyluciferin substrate: new insights into the conformational effect. *Phys. Chem. Chem. Phys.* **2016**, *18*, 27460-27467.

[38] Miertuˇs, S.; Scrocco, E.; Tomasi, J. Electrostatic interaction of a solute with a continuum. A direct utilizaion of AB initio molecular potentials for the prevision of solvent effects. *Chem. Phys.* **1981**, *55*, 117–129.

[39] Garcia-Iriepa, C.; Zemmouche, M.; Ponce-Vargas, M.; Navizet, I. The role of solvation models on the computed absorption and emission spectra: the case of fireflies oxyluciferin. *Phys. Chem. Chem. Phys.* **2019**, *21*, 4613-4623.

[40] Reed, A. E.; Curtiss, L. A.; Weinhold, F. Intermolecular interactions from a natural bond orbital, donor–acceptor viewpoint. *Chem. Rev.* **1988**, *88*, 899–962.

[41] Vriend, G. WHAT IF: A molecular modeling and drug design program. *J. Mol. Graph.* **1990**, *8*, 52–56.

[42] Morris, G. M.; Goodsell, D. S.; Halliday, R. S.; Huey, R.; Hart, W. E.; Belew, R. K.; Olson, A. J. Automated docking using a Lamarckian genetic algorithm and an empirical binding free energy function. *J. Comput. Chem.* **1998**, *19*, 1639–1662.

[43] Berendsen, H. J.; van der Spoel, D.; van Drunen, R. GROMACS: a message-passing parallel molecular dynamics implementation. *Comput. Phys. Commun.* **1995**, *91*, 43–56.

[44] Oostenbrink, C.; Villa, A.; Mark, A. E.; van Gunsteren, W. F. A biomolecular force field based on the free enthalpy of hydration and solvation: The GROMOS force-field parameter sets 53A5 and 53A6. *J. Comput. Chem.* **2004**, *25*, 1656-1676.

[45] Schüttelkopf, A. W.; van Aalten, D. M. F. PRODRG: a tool for high-throughput crystallography of protein-ligand complexes. *Acta Crystal. D* **2004**, *60*, 1355–1363.

[46] Lemkul, J. A.; Allen, W. J.; Bevan, D. R. Practical Considerations for Building GROMOS-Compatible Small-Molecule Topologies. *J. Chem. Inf. Model.* **2010**, *50*, 2221-2235.

[47] Berendsen, H. J. C.; Postma, J. P. M.; van Gunstetren, W. F.; Hermans, J. In *Intermolecular Forces;* Pullman, B., Eds.; Reidel: Dordrecht, The Netherlands, 1981; pp 331-342.

[48] Lemak, A.; Balabaev, N. On the Berendsen thermostat. *Mol. Simul.* **1994**, *13*, 177–187.

[49] Parrinello, M.; Rahman, A. Polymorphic transitions in single crystals: a new molecular dynamics method. *J. Appl. Phys.* **1981**, *52*, 7182–7190.

[50] Rahman, A.; Stillinger, F. H. Molecular dynamics study of liquid water. *J. Chem. Phys.* **1971**, *55*, 3336–3359.

[51] Darden, T.; York, D.; Pedersen, L. Particle mesh Ewald: an N· log (N) method for Ewald sums in large systems. *J. Chem. Phys.* **1993**, *98*, 10089–10092.

[52] Essmann, U.; Perera, L.; Berkowitz, M. L.; Darden, T.; Lee, H.; Pedersen, L. G. A smooth particle mesh Ewald method. *J. Chem. Phys.* **1995**, *103*, 8577–8593.

[53] Dapprich, S.; Komáromi, I.; Byun, K. S.; Morokuma, K.; Frisch, M. J. A new ONIOM implementation in Gaussian98. Part I. The calculation of energies, gradients, vibrational frequencies and electric field derivatives. *J. Mol. Struct.* **1999**, *462*, 1-21.

[54] Vreven, T.; Byun, K. S.; Komáromi, I.; Dapprich, S.; Montgomery, Jr.; Morokuma, K.; Frisch, M. J. Combining quantum mechanics methods with molecular mechanics methods in ONIOM. *J. Chem. Theory Comput.* **2006**, *2*, 815–826.

[55] Min, C. G.; Liu, Q. B.; Leng, Y.; Magalhães, C. M.; Huang, S. J.; Liu, C. X.; Yang, X. K.; Pinto da Silva, L. Mechanistic Insight into the Chemiluminescent Decomposition of *Cypridina* Dioxetanone and the Chemiluminescent, Fluorescent Properties of the Light Emitter of *Cypridina* Bioluminescence. *J. Chem. Inf. Model.* **2019**, *59*, 4393-4401.

[56] Min, C. G.; Pinto da Silva, L.; Esteves da Silva, J. C. G.; Yang, X. K.; Huang, S. J.; Ren, A. M.; Zhu, Y. Q. A Computational Investigation of the Equilibrium Constants for the Fluorescent and Chemiluminescent States of Coelenteramide. *Chem. Phys. Chem.* **2017**, *18*, 117-123.

[57] Frisch, M. J.; Trucks, G. W.; Schlegel, H. B.; Scuseria, G. E.; Robb, M. A.; Cheeseman, J. R.; Scalmani, G.; Barone, V.; Petersson, G. A.; Nakatsuji, H.; et al. GAUSSIAN 16, Revision C. 01, Gaussian, Inc., Wallingford, CT, 2016.

[58] Topol, I. A.; Tawa, G. J.; Burt, S. K.; Rashin, A. A. On the structure and thermodynamics of solvated monoatomic ions using a hybrid solvation model. *J. Chem. Phys.* **1999**, *111*, 10998–11014.

[59] Tuttle, T. R.; Malaxos, S.; Coe, J. V. A new cluster pair method of determining absolute single ion solvation energies demonstrated in water and applied to ammonia. *J. Phys. Chem. A* **2002**, *106*, 925–932.

[60] Bennaim, A.; Marcus, Y., Solvation thermodynamics of nonionic solutes. *J. Chem. Phys.* **1984**, *81*, 2016–2027.

[61] Catalan, J. Spectro-thermodynamic relationship of cationic vs anionic species derived from protonation vs deprotonation of pyrrolo-aza-aromatic bases in homologous series. *J. Am. Chem. Soc.* **2001**, *123*, 11940–119444.

[62] Martin, R. L. Natural Transition Orbitals. *J. Chem. Phys.* **2003**, *118*, 4775–4777.

[63] Li, X.; Frisch, M. J. Energy-represented direct inversion in the iterative subspace within a hybrid geometry optimization method *J. Chem. Theory Comput.* **2006**, *2*, 835–839.

[64] Campetella, M.; Sanz García, J. Following the evolution of excited states along photochemical reaction pathways. *J. Comput. Chem.* **2020**, DOI: 10.1002/jcc.26162.

[65] Sanz García, J.; Boggio-Pasqua, M.; Ciofini, I.; Campetella, M. Excited state tracking during the relaxation of coordination compounds. *J. Comput. Chem*. **2019,** *40*, 1420-1428.

[66] Kasha, M. Characterization of Electronic Transitions in Complex Molecules. *Discuss. Farad. Soc.* **1950**, *9*, 14-19.

TOC Graphic